

# Gravitational lensing by non-self-intersecting vortons

Leonardus B. Putra<sup>\*†</sup>

*Mathematical Institute, University of Oxford, Radcliffe Observatory,  
Andrew Wiles Building, Woodstock Rd, Oxford OX2 6GG*

H. S. Ramadhan<sup>‡</sup>

*Departemen Fisika, FMIPA, Universitas Indonesia, Depok, 16424, Indonesia.*

## Abstract

We present exact solutions to the Nambu-Goto equations for thin vortons stabilized by chiral currents. The solutions describe a class of non-self-intersecting, stationary loops with arbitrary shapes. In addition to the trivial circular and the Kibble-Turok vortons, we also derive a two-parameter family that incorporates the first, second, and third harmonic modes. We found that, in general, the vorton's constraints allow for constructing families of solutions with arbitrary harmonic modes. We further investigate the gravitational lensing effects associated with these solutions under the weak-field and thin-lens approximations. For circular vortons, the lensing exhibits a sharp discontinuity separating two regions with distinctly different distortions. The corresponding Einstein ring co-exist alongside an almost undistorted source image. This effect is significantly amplified in the case of non-circular vortons, highlighting their potential observational signatures.

---

\* Corresponding author.

†Electronic address: leonardus.putra@exeter.ox.ac.uk

‡Electronic address: hramad@sci.ui.ac.id

## I. INTRODUCTION

Scientific interest in ring-shaped celestial objects dates back over four centuries, beginning with Galileo's observation of Saturn's rings [1, 2]. Gauss demonstrated that the gravitational potential around a circular ring can be described using elliptic functions [3]. Maxwell showed that Saturn's rings would be unstable if they consisted of a solid mass or a continuous fluid [4]. The orbital dynamics and stability around a circular ring in Newtonian gravity are explored in works such as [5] and the references therein.

The ring's orbital dynamics becomes richer when considered within the framework of general relativity. One of the most well-known (albeit hypothetical) cosmological object with  $S^1$  topology is the cosmic string loop [6, 7]. The enormous tension forces the loop to oscillate. The non-stationary metric around a circular loop was studied in [8–10], where external mechanisms must be introduced to prevent it from collapsing.

In the thin-string approximation the dynamics of relativistic loops is governed by the Nambu-Goto equation [11, 12], whose general solutions can be expanded in the Fourier modes. By considering the first and third harmonics, Kibble and Turok [13, 14] found a class of two-parameter family of smooth exact closed-loop solutions that never self-intersect. Generalizations to a third-parameter family or involving arbitrary number of harmonics were discussed in [15, 16]. The gravitational lensing by some of these loops has been investigated by De Laix and Vachaspati [17].

If current is allowed to flow along the string loop, it can generate angular momentum that counteracts its tendency to oscillate. This stable, stationary configuration is known as a *vorton* [18]. Their formation, dynamics, stability, and cosmological significance have extensively been studied, for example, in [19–25]. In [26] we examine the metric around a circular vorton stabilized by a chiral current in the weak-field limit. The resulting metric functions are analogous to the 4-potential generated by a circular current-carrying wire loop. Asymptotically, the metric reduces to that of a Kerr black hole with mass  $M = 4\pi R\mu$ , with  $R$  the radius and  $\mu$  the tension. We found that for a typical GUT-scale string the extremal Kerr bound is always saturated. This implies that, to a distant observer, a GUT-scale vorton would be indistinguishable from a Kerr naked singularity.

The present paper aims to extend our previous analysis to vortons with arbitrary shapes, including both circular and non-circular configurations. This generalization, however, comes

at the cost of losing the explicit form of the metric. To address this, we employ the thin-lens approximation. In Section II we introduce the general solutions for vorton loops and discuss their non-self-intersection constraints. In Section III we calculate the corresponding deflection vectors and magnifications of the thin lens formalism. We then illustrate the lensing images of milky way galaxy caused circular and non-circular vortons. Finally, in Section IV we summarize our findings and provide concluding remarks.

## II. VORTON SOLUTIONS

### A. Chiral String Loops

The position of a string over time is described by the three-vector  $\vec{x}(\zeta, t)$ , which satisfies the flat-spacetime Nambu-Goto equations in conformal gauge:

$$\begin{aligned}\ddot{\vec{x}} - \vec{x}'' &= 0, \\ \dot{\vec{x}} \cdot \vec{x}' &= 0, \\ \dot{\vec{x}}^2 + \vec{x}'^2 &= 1.\end{aligned}\tag{1}$$

The general solution to these equations is given by

$$\vec{x} = \frac{1}{2} \left[ \vec{a}(\zeta - t) + \vec{b}(\zeta + t) \right],\tag{2}$$

where  $\vec{a}$  and  $\vec{b}$  are traveling wave functions satisfying  $\vec{a}'^2 = \vec{b}'^2 = 1$ .

Vorton is a superconducting string loop whose current generates angular momentum that counteracts its tendency to collapse. The current can either be electromagnetic or chiral. Carter and Peter showed that in the chiral limit the superconducting string's dynamics can be simplified [27]. They proposed the following action

$$S = \int d^2\zeta \left( -\mu\sqrt{-\gamma} + \frac{1}{2}\sqrt{-\gamma}\gamma^{ab}\varphi_{,a}\varphi_{,b} \right).\tag{3}$$

The chiral condition  $\varphi_{,a}\varphi^{,a} = 0$  acts as a constraint, and the equations of motion (EoM) are

$$\partial_a (\mathcal{T}^{ab}x_{,b}^\nu) = 0, \quad \partial_a (\sqrt{-\gamma}\gamma^{ab}\varphi_{,b}) = 0,\tag{4}$$

where

$$\mathcal{T}^{ab} \equiv \sqrt{-\gamma} (\mu\gamma^{ab} + \theta^{ab}), \quad \theta_{ab} \equiv \varphi_{,a}\varphi_{,b}, \quad (5)$$

are the string worldsheet and charge carrier energy-momentum tensors, respectively.

It is convenient to choose a gauge so that

$$\mathcal{T}^{ab} = \mu\eta^{ab}, \quad (6)$$

which is satisfied for the chiral case. In this gauge, the EoM becomes similar to that of Nambu-Goto strings Eq. (2),

$$\ddot{\vec{x}} - \vec{x}'' = 0, \quad \ddot{\varphi} - \varphi'' = 0, \quad (7)$$

whose solutions are

$$\vec{x} = \frac{1}{2}(\vec{a}(\zeta - t) + \vec{b}(\zeta + t)), \quad \varphi(\sigma, \tau) = F(\sigma + \tau). \quad (8)$$

For the chiral string case, however, the constraints become

$$|\vec{a}'| = 1, \quad |\vec{b}'|^2 \equiv k^2 = 1 - \frac{4F'^2}{\mu}. \quad (9)$$

Expanding the traveling waves in Fourier modes, with  $L \equiv 2\pi R$  and integrating them over  $0 \leq \zeta_{\pm} \leq L$  yields

$$\sum_{n=1}^{\infty} n^2 (|\vec{a}_n^-|^2 + |\vec{b}_n^-|^2) = 2, \quad \sum_{n=1}^{\infty} n^2 (|\vec{a}_n^+|^2 + |\vec{b}_n^+|^2) = 2k^2. \quad (10)$$

For the Nambu-Goto strings, we have  $k = 1$ , while for the vorton solutions, we have  $k = 0$ .

## B. Circular Vorton

It is easy to show that the following parametrizations

$$\vec{a}_n^- = \frac{\delta_{nm}}{m} (0, \cos \phi, \sin \phi), \quad \vec{b}_n^- = \frac{\delta_{nm}}{m} (1, 0, 0), \quad (11)$$

$$\vec{a}_n^+ = k \frac{\delta_{nm}}{m} (0, \cos \phi, \sin \phi), \quad \vec{b}_n^+ = k \frac{\delta_{nm}}{m} (1, 0, 0), \quad (12)$$

with  $m$  integers are solutions of Eqs. (10). Following the convention used in Ref. [20], and rescaling  $R \rightarrow mR$ , we write

$$\begin{aligned} \vec{a}(q) &= R \left( \cos \frac{q}{R}, \cos \phi \sin \frac{q}{R}, \sin \phi \sin \frac{q}{R} \right), \\ \vec{b}(\eta) &= kR \left( \cos \frac{\eta}{R}, \cos \phi \sin \frac{\eta}{R}, \sin \phi \sin \frac{\eta}{R} \right), \end{aligned} \quad (13)$$

with  $q \equiv t + \sigma$ ,  $\eta \equiv t - \sigma$ , and  $\sigma$  the string's worldsheet spacelike coordinate.

This family of solutions describes a circular string loop oscillating between radius of  $(1 - k)R/2$  and  $(1 + k)R/2$ , tilted with an angle  $\phi$  around the  $x$  axis. The Nambu-Goto limit of this family can be found by setting  $k = 1$ ,

$$\vec{r} = R \cos \frac{t}{R} \left( \cos \frac{\sigma}{R}, \cos \phi \sin \frac{\sigma}{R}, \sin \phi \sin \frac{\sigma}{R} \right), \quad (14)$$

describing an oscillating circular string loop of maximum radius  $R$  without current. The stationary, or ‘‘vorton’’, limit arises by setting  $k = 0$  and rescaling  $R \rightarrow 2R$ , leading to

$$\vec{r} = R \left( \cos \frac{q}{2R}, \cos \phi \sin \frac{q}{2R}, \sin \phi \sin \frac{q}{2R} \right), \quad (15)$$

which describes a circular vorton with radius  $R$ .

## C. Kibble-Turok Vorton

Kibble and Turok[13, 14] presented a class of string loop solutions by considering the first and third harmonics. If the string is chiral, then we set  $k = 1$  in (9). This Kibble-Turok

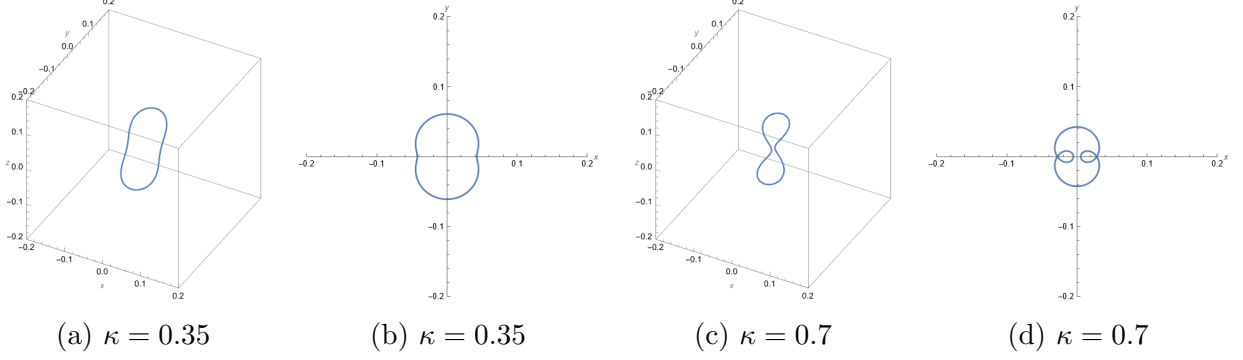


FIG. 1: Parametric 3D (a, c) and top-view (b, d) curves of Kibble-Turok vorton solutions of various  $\kappa$ .

chiral loop reads

$$\begin{aligned}
\vec{a}_1^- &= (1 - \kappa, 0, 0), & \vec{b}_1^- &= \left(0, -(1 - \kappa), -2\sqrt{\kappa(1 - \kappa)}\right), \\
\vec{a}_3^- &= \left(\frac{1}{3}\kappa, 0, 0\right), & \vec{b}_3^- &= \left(0, -\frac{1}{3}\kappa, 0\right), \\
\vec{a}_1^+ &= (1, 0, 0), & \vec{b}_1^+ &= (0, -\cos \phi, -\sin \phi),
\end{aligned} \tag{16}$$

where  $0 < \kappa \leq 1$  and  $-\pi \leq \phi \leq \pi$  are constant parameters. We can generalize this result for the case of  $k \neq 0$  by setting

$$\vec{a}_1^+ = k(1, 0, 0), \quad \vec{b}_1^+ = k(0, -\cos \phi, -\sin \phi). \tag{17}$$

Using the same convention as in Eq. (13) and setting  $L = 2\pi R$ , we get

$$\begin{aligned}
\vec{r} = \frac{R}{2} &\left[ (1 - \kappa) \sin \frac{q}{R} + \frac{1}{3}\kappa \sin \frac{3q}{R} + k \sin \frac{\eta}{R}, \right. \\
&- \left( (1 - \kappa) \cos \frac{q}{R} + \frac{1}{3}\kappa \cos \frac{3q}{R} + k \cos \phi \cos \frac{\eta}{R} \right), \\
&\left. - \left( 2\sqrt{\kappa(1 - \kappa)} \cos \frac{q}{R} + k \sin \phi \cos \frac{\eta}{R} \right) \right]. \tag{18}
\end{aligned}$$

It should be noted that the limit of  $\kappa = 0$  and  $\phi = 0$  brings the solution back to the circular case.

The Kibble-Turok vorton can be obtained by taking  $k = 0$  and  $R \rightarrow 2R$ , which yields

$$\vec{r} = R \left[ (1 - \kappa) \sin \frac{q}{2R} + \frac{1}{3} \kappa \sin \frac{3q}{2R}, -(1 - \kappa) \cos \frac{q}{2R} - \frac{1}{3} \kappa \cos \frac{3q}{2R}, -2\sqrt{\kappa(1 - \kappa)} \cos \frac{q}{2R} \right]. \quad (19)$$

Since the dependence on  $\phi$  couples to  $k$ , the Kibble-Turok vorton is parametrized by only one parameter,  $\kappa$ . In Fig. 1 we show Kibble-Turok vorton profiles for several  $\kappa$ .

#### D. The 123-harmonic Vorton

While the original Kibble-Turok solution considers only the first and third non-zero harmonics, our vorton loop formalism allows the inclusion of all harmonic modes. Here, we construct a vorton loop that includes the first, second, and third harmonics, referred to as *the 123-vorton* for short, given by

$$\begin{aligned} \vec{a}_1^- &= \left( \sqrt{\beta}(1 - \kappa), 0, 0 \right), & \vec{b}_1^- &= \left( 0, -\sqrt{\beta}(1 - \kappa), -2\sqrt{\kappa(1 - \kappa)} \right), \\ \vec{a}_2^- &= \left( 0, \frac{1}{\sqrt{2}} \sqrt{1 - 2\beta - \kappa^2}, 0 \right), & \vec{b}_2^- &= \left( 0, \sqrt{\frac{\beta}{2}}, \kappa \sqrt{\frac{\beta}{2}} \right), \\ \vec{a}_3^- &= \left( \frac{1}{3} \kappa, 0, 0 \right), & \vec{b}_3^- &= \left( 0, -\frac{1}{3} \kappa, 0 \right), \end{aligned} \quad (20)$$

with the  $\zeta_+$  terms remaining as in the Kibble-Turok solution

$$\vec{a}_1^+ = k(1, 0, 0), \quad \vec{b}_1^+ = k(0, -\cos \phi, -\sin \phi). \quad (21)$$

As in the Kibble-Turok vorton, we have  $0 < \kappa \leq 1$  and  $-\pi \leq \phi \leq \pi$ . The parameter  $\beta$  is introduced to incorporate the second harmonic into the solution, with  $0 < \beta \leq \frac{1}{2}(1 - \kappa^2)$ . This solution, however, is not an exact generalization of the Kibble-Turok solution, as the Kibble-Turok solution cannot be fully recovered by setting a specific value of  $\beta$ .

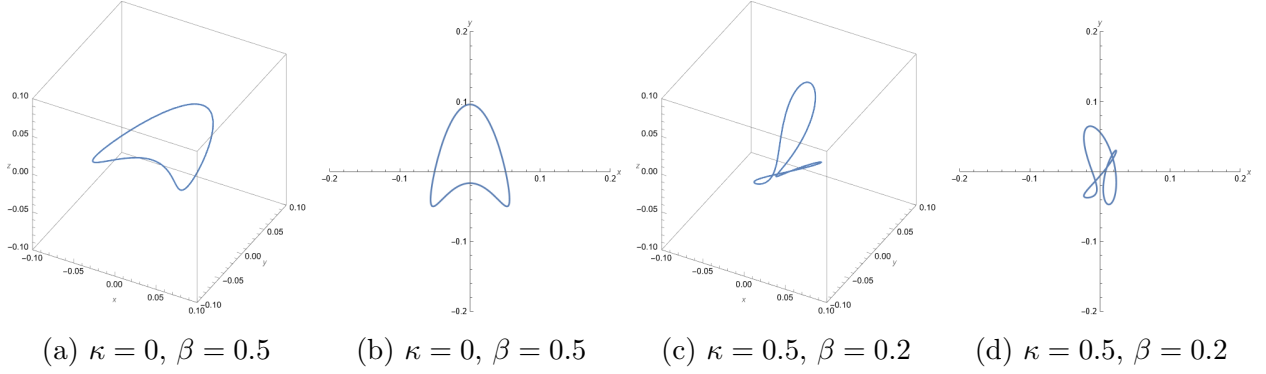


FIG. 2: Parametric 3D (a, c) and top-view (b, d) curves of the 123 vorton solutions of various  $\kappa$  and  $\beta$ .

The 123-vorton then describes a class of two-parameter family of solution given by

$$\begin{aligned} \vec{r} = R & \left[ \sqrt{\beta}(1 - \kappa) \sin \frac{q}{2R} + \frac{1}{3}\kappa \sin \frac{3q}{2R}, \right. \\ & - \left( \sqrt{\beta}(1 - \kappa) \cos \frac{q}{2R} - \frac{1}{\sqrt{2}}\sqrt{1 - 2\beta - \kappa^2} \sin \frac{q}{R} - \sqrt{\frac{\beta}{2}} \cos \frac{q}{R} + \frac{1}{3}\kappa \cos \frac{3q}{2R} \right), \\ & \left. \kappa\sqrt{\frac{\beta}{2}} \cos \frac{q}{R} - 2\sqrt{\kappa(1 - \kappa)} \cos \frac{q}{2R} \right], \end{aligned} \quad (22)$$

parametrized by  $\kappa$  and  $\beta$ . The solutions are shown in Fig. 2 for various values of  $\kappa$  and  $\beta$ .

### E. Self-intersection and Additional Constraints

Strings can intersect and interact with themselves. Imposing a non-self-intersection condition introduces additional constraints on our solutions. The solution  $\vec{r}$  will self-intersect if and only if  $\exists \alpha \in (0, 2\pi)$  &  $\theta \in [0, 2\pi]$  such that

$$\vec{r}(\theta + \alpha) = \vec{r}(\theta). \quad (23)$$

The circular Nambu-Goto string loop and vorton solutions, Eq. (14)-(15), are inherently circular and, therefore, do not self-intersect. It is worth noting that the definition of self-intersection used in this study is slightly different from that in [20]. Here, the self-intersection refers to configurations where the string continuously intersects itself at fixed point (stationary intersection). In contrast, Ref. [20] defines the self-intersection to be configurations



where the loop intersects itself at some specific time  $t$  (dynamic intersection).

To ensure a non-self-intersecting Kibble-Turok vorton, we impose the additional constraint

$$0 < \kappa < 3/4, \quad (24)$$

where  $\kappa = 0$  corresponds to the circular loop.

And for the 123-vorton:

$$\frac{3}{4\kappa}(\sqrt{\beta} - \kappa\sqrt{\beta} + \kappa) \neq 1, \quad 1 - 2\beta - \kappa^2 \neq 0. \quad (25)$$

### III. LENSING OF VORTON

#### A. Thin Lens Formalism

Gravitational lensing by string loop can be computed using the thin lens approximation, where lensing takes place at a specific moment in time  $t_0$ , alongside the weak-field approximation of linearized gravity, as utilized in [17]. This formalism can be split into two main components. The first is the deflection vector, which constructs the lensing image. The second component is the magnification, which defines the curve of infinite magnification (the critical curve) and quantifies the image scale.

The deflection of photon from its flat spacetime trajectory is described by  $\vec{\alpha}$ , which represents the change in the photon's velocity vector due to lensing. This can be expressed as

$$\vec{\alpha} = -4G\mu \int d\sigma \left( \frac{F_{\mu\nu}(\sigma, t)\gamma^\mu\gamma^\nu \vec{f}_\perp}{1 - \dot{f}_\parallel} \frac{\vec{f}_\perp}{f_\perp^2} \right)_{t=t_0}, \quad (26)$$

with

$$F_{\mu\nu} \equiv \dot{f}_\mu \dot{f}_\nu - f'_\mu f'_\nu - \eta_{\mu\nu} \dot{f}^2, \quad (27)$$

$\gamma^\mu$  the four-velocity of the light ray,  $f_\mu$  the parameterized coordinate of the string loop, and  $t_0$  the solution of  $f_\parallel(t_0, \sigma) = t_0$ . The lensing is governed by the famous Virbhadra-Ellis lens equation [28]

$$\vec{\eta} = \frac{D_s}{D_l} \vec{\xi} - D_{ls} \vec{\alpha}(\vec{\xi}), \quad (28)$$

where  $D_l$  is the distance from observer to the lens,  $D_s$  is the distance from the observer to

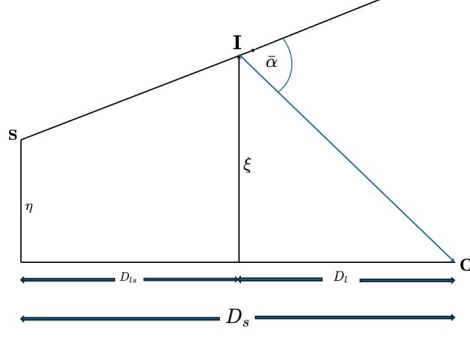


FIG. 3: Lensing Diagram in Thin Lens Approximation.

source, and  $D_{ls}$  the distance from the lens to source. The lens diagram is shown in Fig.3, where

$$\vec{\alpha}(\vec{x}) = \vec{\alpha}(\xi) \frac{D_{ls} D_l}{D_s R}. \quad (29)$$

From Eq. (27), we have

$$F_{\mu\nu} \gamma^\mu \gamma^\nu = \left(1 - \dot{\vec{f}} \cdot \hat{\gamma}\right)^2 - \left(-\vec{f}' \cdot \hat{\gamma}\right)^2, \quad (30)$$

with  $\hat{\gamma}$  the spatial unit vector of  $\gamma^\mu$ . The vector  $\vec{f}$  represents the displacement from the light ray's position in the lensing plane (at  $t_0$ ) to the parametric four-coordinate of the string loop. Taking the string loop's center of mass as the origin, the 3-vector  $\vec{f}$  can be decomposed as  $\vec{f} = \vec{r} - \vec{x}_0$ , where  $\vec{r}$  is the coordinate of the string loop, and  $\vec{x}_0$  is the light ray coordinate at  $t_0$ . This vector  $\vec{f}$  can be further decomposed (with respect to the optical axis) into the perpendicular and parallel components

$$\vec{f}_\perp = \vec{r}_\perp - \vec{\zeta}, \quad \vec{f}_\parallel = \vec{r} \cdot \hat{\gamma} - \vec{x}_0 \cdot \hat{\gamma}, \quad (31)$$

with  $\vec{\zeta}$  the perpendicular component of  $\vec{x}_0$ . Thus, we have

$$\dot{f}_\parallel = \frac{d}{dt} (\vec{r} \cdot \hat{\gamma}) = \dot{r}_\gamma. \quad (32)$$

Here  $r_\gamma$  is the string loop vector component parallel to the optical axis. We then have

$$\vec{\alpha} = -4G\mu \frac{D_{l_s} D_l}{R D_s} \int d\sigma \left[ \frac{(1 - \dot{r}_\gamma)^2 - r_\gamma'^2}{1 - \dot{r}_\gamma} \frac{\vec{r}_\perp - \vec{\zeta}}{(\vec{r}_\perp - \vec{\zeta})^2} \right]_{t=t_0}. \quad (33)$$

We can re-parametrize  $\vec{\zeta}$  and  $\vec{r}_\perp$  as

$$\vec{\zeta} = R(x_1 \hat{e}_1 + x_2 \hat{e}_2), \quad \vec{r}_\perp = R \left( \frac{r_1}{R} \hat{e}_1 + \frac{r_2}{R} \hat{e}_2 \right). \quad (34)$$

Choosing the optical axis to be  $\hat{e}_3$  along with the light ray direction  $\hat{\gamma} = \hat{e}_3$  (assuming small deflection angle), we have

$$\vec{\alpha} = C \vec{F}, \quad (35)$$

with

$$C \equiv 8\pi G\mu \frac{D_{l_s} D_l}{R D_s}, \quad (36)$$

a constant, and

$$\vec{F} \equiv F_1(x_1, x_2) \hat{e}_1 + F_2(x_1, x_2) \hat{e}_2, \quad (37)$$

the deflection vector, where

$$F_1(x_1, x_2) \equiv -\frac{1}{2\pi} \int \frac{d\sigma}{R} \left[ \frac{(1 - \dot{r}_\gamma)^2 - r_\gamma'^2}{1 - \dot{r}_\gamma} \frac{\frac{r_1}{R} - x_1}{\left(\frac{r_1}{R} - x_1\right)^2 + \left(\frac{r_2}{R} - x_2\right)^2} \right]_{t=t_0},$$

$$F_2(x_1, x_2) \equiv -\frac{1}{2\pi} \int \frac{d\sigma}{R} \left[ \frac{(1 - \dot{r}_\gamma)^2 - r_\gamma'^2}{1 - \dot{r}_\gamma} \frac{\frac{r_2}{R} - x_2}{\left(\frac{r_1}{R} - x_1\right)^2 + \left(\frac{r_2}{R} - x_2\right)^2} \right]_{t=t_0} \quad (38)$$

The lens equation therefore becomes

$$y_1 = x_1 - C F_1(x_1, x_2),$$

$$y_2 = x_2 - C F_2(x_1, x_2). \quad (39)$$

The rescaled coordinates  $\vec{y}$  and  $\vec{x}$  are the source and the image positions, respectively.

The magnification of the transformed (mapped) image is given by [29]:

$$M = \frac{1}{\det J(x_1, x_2)}, \quad (40)$$

where  $J_{ij}(x_1, x_2)$  is the Jacobian of Eq. (39). Thus,

$$M = \frac{1}{(1 - CF_{1,1})(1 - CF_{2,2}) - C^2 F_{1,2} F_{2,1}}, \quad (41)$$

where  $F_{i,j} \equiv \partial F_i / \partial x_j$ . The critical curve, defined as the curve with infinite magnification, is just the curve  $(x_1, x_2)$  satisfying

$$(1 - CF_{1,1})(1 - CF_{2,2}) - C^2 F_{1,2} F_{2,1} = 0. \quad (42)$$

Since Eqs. (39) map  $\vec{x} \rightarrow \vec{y}$ , the caustic images are obtained by substituting the solution of Eq. (42) into Eq. (39).

## B. Circular Vorton and Nambu-Goto Loops

Here, we apply the formalism to the case of the circular vorton given by Eq. (15). For comparison, we also apply it to the circular Nambu-Goto loop (14), as both exhibit similar geometries. For the Nambu-Goto loop, we define the coordinate  $\sigma \equiv R\theta$  and let  $r_o(t) = \cos t/R$ . At the time of maximum loop radius,  $t_0 = 0$ , we set  $r_o(t_0) = 1$ . This set up leads to

$$\begin{aligned} F_1(x_1, x_2) &= -\frac{1}{2\pi} \int_0^{2\pi} d\theta \frac{(1 - \sin^2 \phi \cos^2 \theta) (\cos \theta - x_1)}{(\cos \theta - x_1)^2 + (\cos \phi \sin \theta - x_2)^2}, \\ F_2(x_1, x_2) &= -\frac{1}{2\pi} \int_0^{2\pi} d\theta \frac{(1 - \sin^2 \phi \cos^2 \theta) (\cos \phi \sin \theta - x_2)}{(\cos \theta - x_1)^2 + (\cos \phi \sin \theta - x_2)^2}. \end{aligned} \quad (43)$$

For the case of circular vorton, we define  $\theta \equiv (t_0 + \sigma)/2R$ . It yields

$$\begin{aligned} F_1(x_1, x_2) &= -\frac{1}{\pi} \int_0^{2\pi} d\theta \left[ \frac{1 - \sin \phi \cos \theta}{1 - \frac{1}{2} \sin \phi \cos \theta} \frac{\cos \theta - x_1}{(\cos \theta - x_1)^2 + (\cos \phi \sin \theta - x_2)^2} \right], \\ F_2(x_1, x_2) &= -\frac{1}{\pi} \int_0^{2\pi} d\theta \left[ \frac{1 - \sin \phi \cos \theta}{1 - \frac{1}{2} \sin \phi \cos \theta} \frac{\cos \phi \sin \theta - x_2}{(\cos \theta - x_1)^2 + (\cos \phi \sin \theta - x_2)^2} \right]. \end{aligned} \quad (44)$$

In the perpendicular direction ( $\phi = 0$ ), both the Nambu-Goto loop and the circular vorton produce the same deflection vector  $\vec{F}$ ; however, the magnitude for the circular vorton is twice that of the Nambu-Goto loop. By rescaling  $C \rightarrow 2C$  or setting  $\mu = 2\mu$  and subsequently dividing the deflection vector by a factor of 2 (which leaves the lens equations unchanged), we obtain an identical deflection vectors for both cases. Thus, the gravitational lensing signatures of a circular Nambu-Goto string and a vorton with linear mass densities  $\mu$  and  $2\mu$ , respectively, are identical when the loop plane is perpendicular to the optical axis. In this study, we set  $C = 2.250$  for the Nambu-Goto loop and  $C = 1.125$  for vortons, ensuring comparable conditions in the circular cases. The density plots in Fig. 4-7 illustrates the components and magnitude of  $\vec{F}$ . Note that the coordinate runs from  $(x_1, x_2) = (-2, -2)$  to  $(x_1, x_2) = (2, 2)$ , with  $x_1$  being the horizontal axis and  $x_2$  the vertical axis.

Figs. 4-5 show that the deflection is symmetric and uniform, in the sense that points near each part of the string projection experiencing similar levels of deflection. In contrast, Figs. 6-7 reveal left-right asymmetry in the deflection vector. Furthermore, the deflection near the string segments where the current is maximally aligned with the source are significantly stronger than in other regions. This phenomenon can be attributed to the fact that the photon has to undergo the frame dragging in the opposite direction of the light ray at those points. For  $\phi = 0$ , both the Nambu-Goto loop and vorton yield identical results, as expected. Additionally, the results show discontinuities at the string projection, arising from the residue theorem in the integral calculation. The observed asymmetry, along with the absence of double imaging of the string, is noteworthy; it likely results from scale differences and the use of the thin-lens approximation.

Figs. 8-9 display density plots of the magnification for the circular Nambu-Goto loop and circular vorton at various values of  $\phi$ . Aside from the symmetry, it is notable that the magnification magnitude near the string is on the order of unity. We can also see that within the string projection, the magnification remains relatively constant and is also around unity. Due to the non-invertibility of the lens equations, there could be multiple images of the same source points. Consequently, an observer might see a relatively undistorted, source-like image (*e.g.*, of a galaxy) alongside more distorted images.

The lensing images of the circular Nambu-Goto string and circular vorton can be effectively compared through their critical curves and caustics. As shown in Figs. 10 and 11, the critical curves and caustics of the circular Nambu-Goto string are symmetric while those of

the circular vorton are asymmetric. This asymmetry arises due to the frame-dragging effect.

In Figs. 12-13 and 14-15 we can visibly observe a discontinuity between the images inside and outside the Nambu-Goto loop and the vorton, respectively. This is a generic feature in the thin-string approximation, which is expected to be smoothed out by the order of string's finite thickness  $\delta$  or by using the full field equations. The difference of symmetry between the Nambu-Goto loop and the vorton case is more apparent, with the circular vorton producing an asymmetric Einstein ring despite its symmetric geometry. On the other hand, the Nambu-Goto loop yields a symmetric Einstein ring.

We can see that the region between the critical curve and the string is the region of inversion, where, as in 12 and 14, the blue circle takes place north of the red circle, where in the unlensed image it takes place south of the red circle, as it is the case of the image inside the string and outside the critical curve. The black region in 14b (and several figures in the following discussions) is present because the image mapping algorithm ran out of pixel to sample from the source plane, in other words the  $\vec{y}$  output is outside the source image.

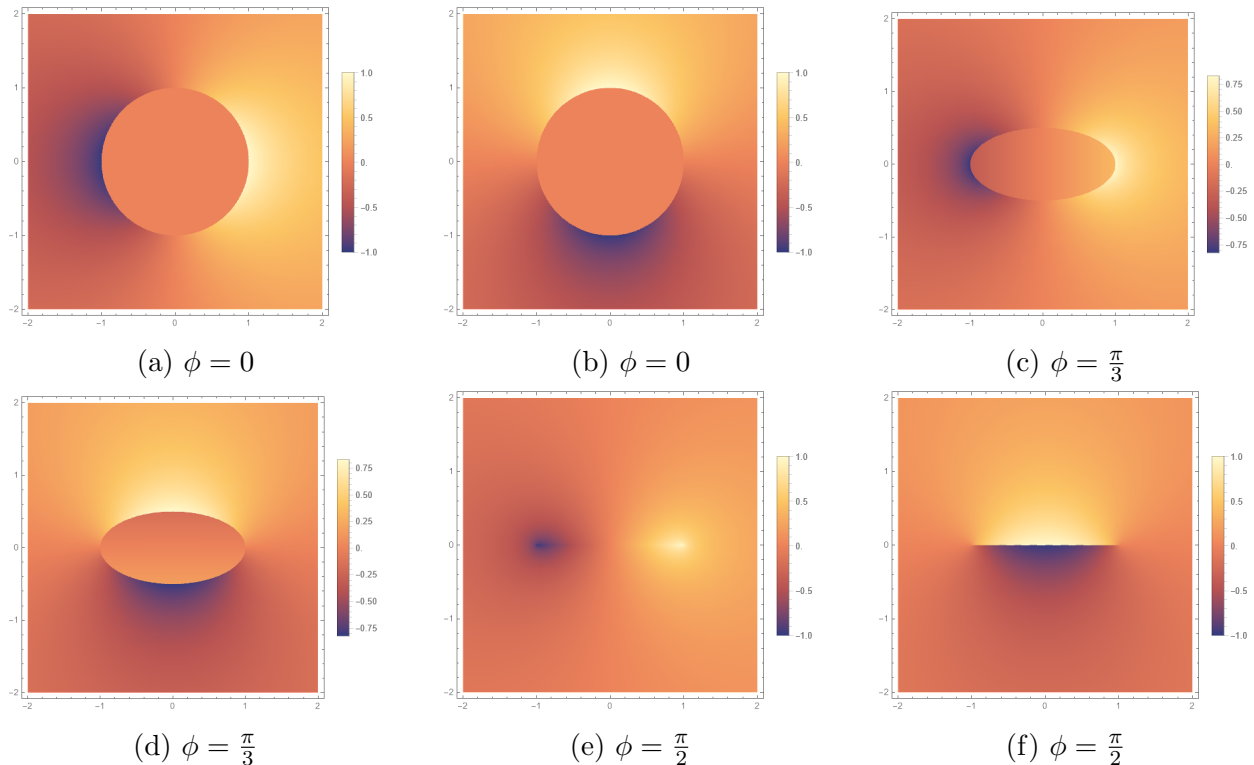


FIG. 4: Deflection vector component  $F_1$  (a, c, e) and  $F_2$  (b, d, f) from circular Nambu-Goto loop of various  $\phi$ .

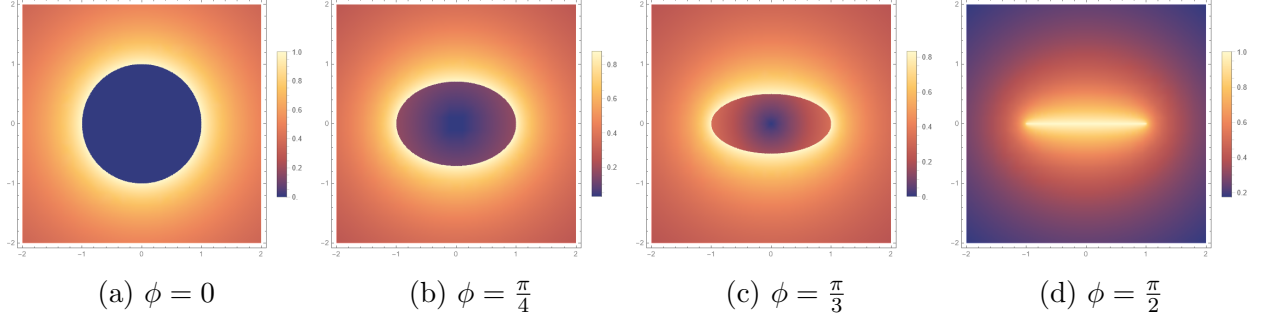


FIG. 5: Deflection vector magnitude  $|\vec{F}| = \sqrt{F_1^2 + F_2^2}$  from circular Nambu-Goto loop for several  $\phi$ .

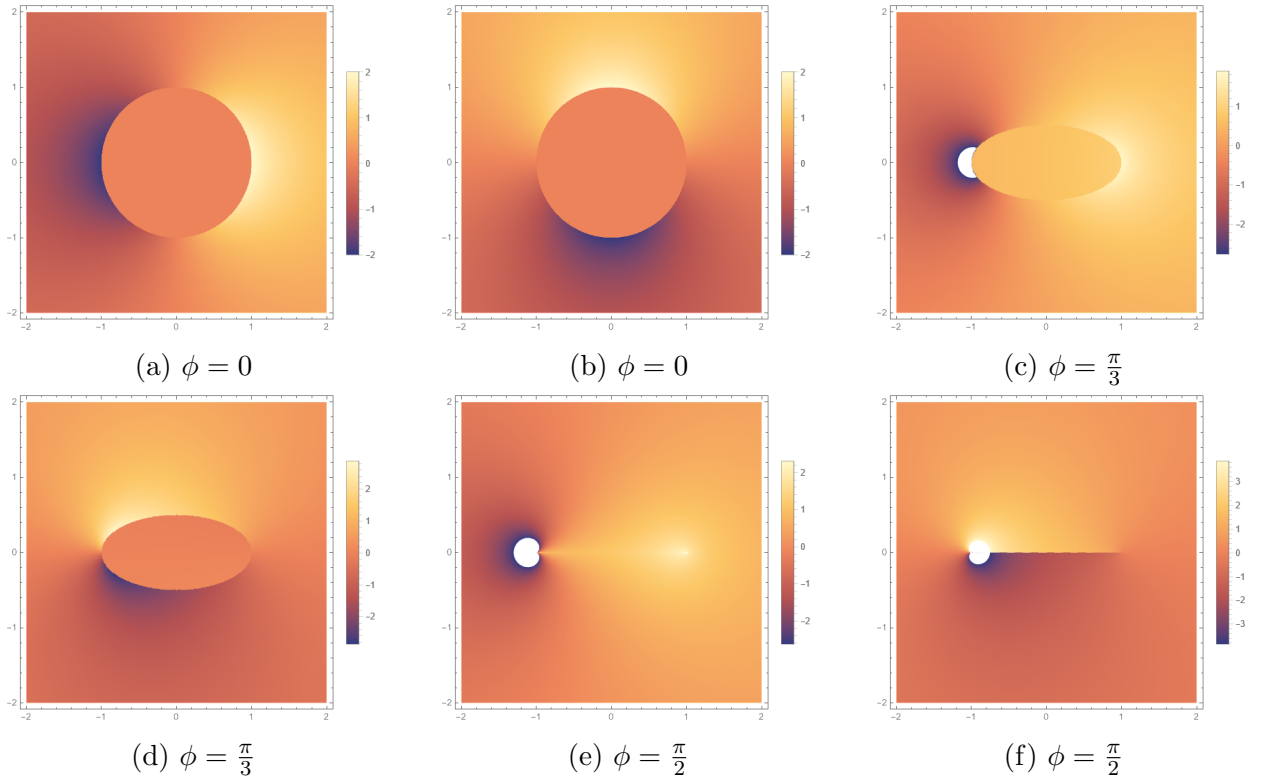


FIG. 6: Deflection vectors  $F_1$  (a, c, e) and  $F_2$  (b, d, f) from circular vorton for several  $\phi$ .

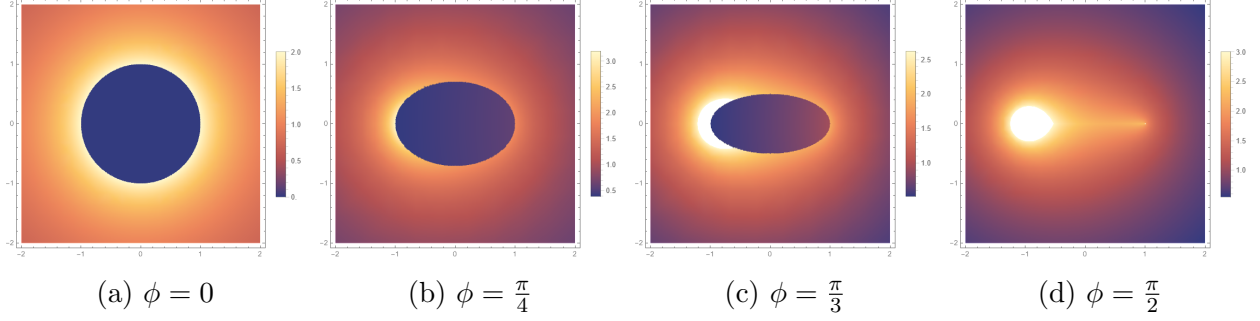


FIG. 7: Deflection vector magnitude  $|\vec{F}| = \sqrt{F_1^2 + F_2^2}$  from circular vorton of various  $\phi$ .

### C. Kibble-Turok Vorton

Starting from the Kibble-Turok vorton in Eq. (19) and redefining  $\theta \equiv (t_0 + \sigma)/2R$ , we obtain the deflection vector components

$$\begin{aligned}
 F_1(x_1, x_2) &= -\frac{1}{\pi} \int_0^{2\pi} d\theta \left( \frac{1 - 2\sqrt{\kappa(1-\kappa)} \sin \theta}{1 - \sqrt{\kappa(1-\kappa)} \sin \theta} \right) \frac{(1-\kappa) \sin \theta + \frac{1}{3}\kappa \sin(3\theta) - x_1}{V}, \\
 F_2(x_1, x_2) &= \frac{1}{\pi} \int_0^{2\pi} d\theta \left( \frac{1 - 2\sqrt{\kappa(1-\kappa)} \sin \theta}{1 - \sqrt{\kappa(1-\kappa)} \sin \theta} \right) \frac{(1-\kappa) \cos \theta + \frac{1}{3}\kappa \cos(3\theta) + x_2}{V}, \quad (45)
 \end{aligned}$$

where

$$V \equiv \left( (1-\kappa) \sin \theta + \frac{1}{3}\kappa \sin(3\theta) - x_1 \right)^2 + \left( (1-\kappa) \cos \theta + \frac{1}{3}\kappa \cos(3\theta) + x_2 \right)^2. \quad (46)$$

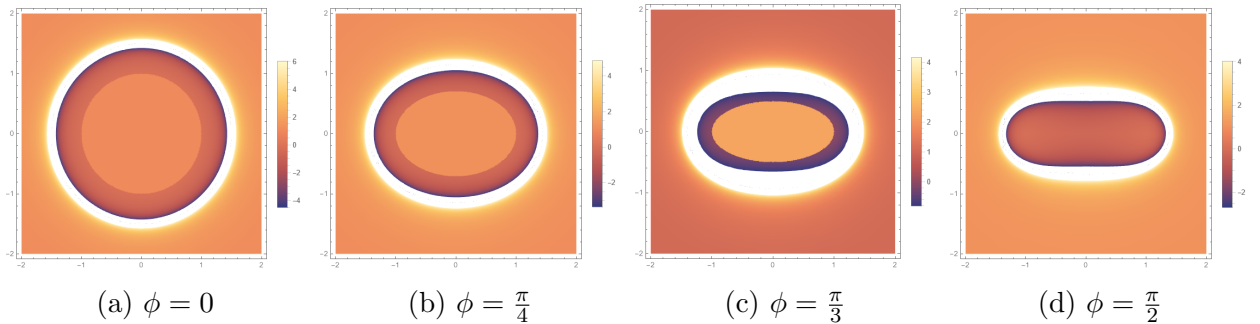


FIG. 8: Magnification by circular Nambu-Goto loop for various  $\phi$ .



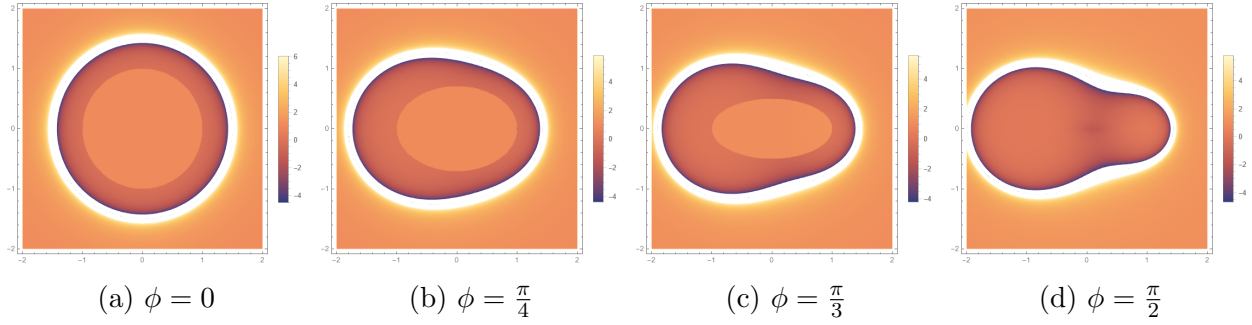


FIG. 9: Magnification by circular vorton for various  $\phi$ .

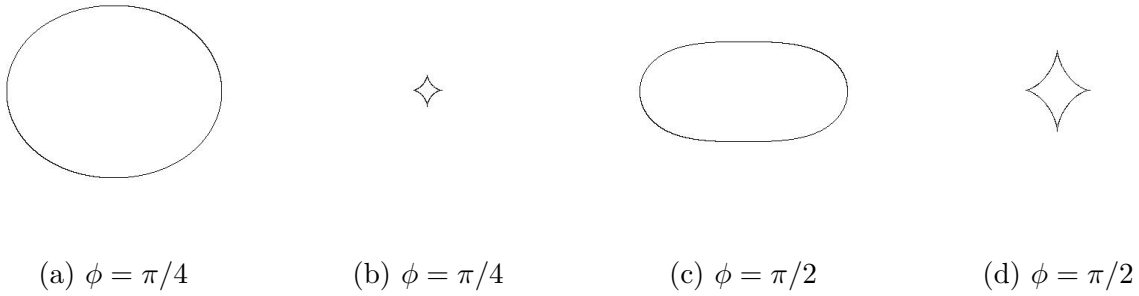


FIG. 10: Critical (a, c) and caustics (b, d) curves of the circular cosmic string of various  $\phi$  at  $t = 0$ .

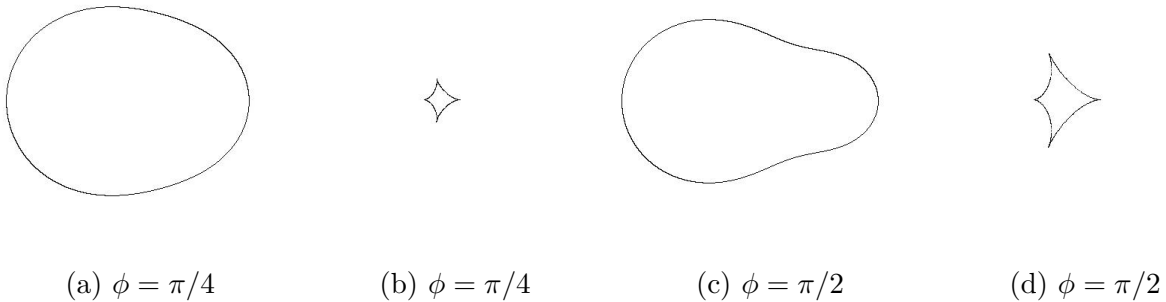


FIG. 11: Critical (a, c) and caustics (b, d) curves of the circular vorton of various  $\phi$ .

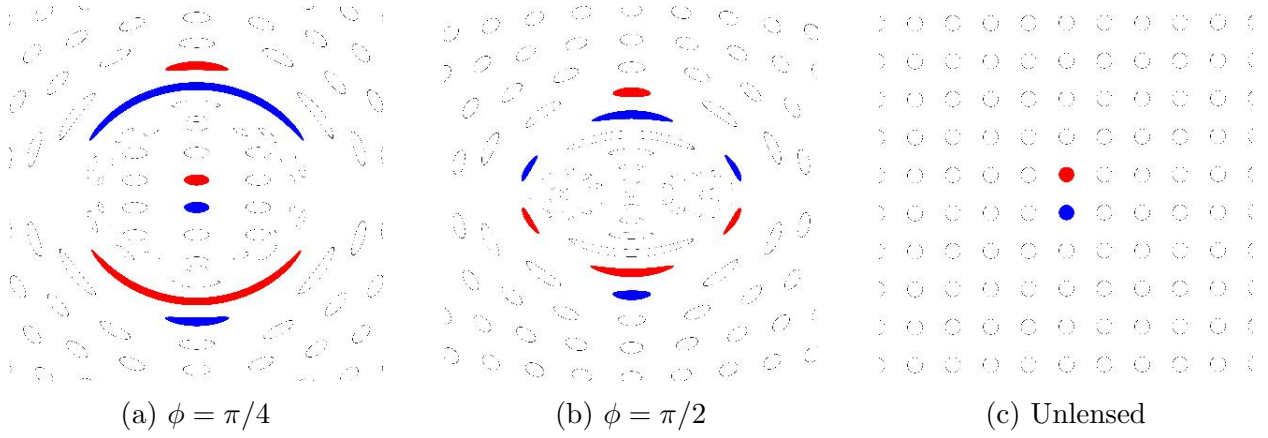


FIG. 12: Lensing Image of circular cosmic string loop at  $\phi = \pi/4$  (a) and  $\phi = \pi/2$  (b) and the unlensed image (c).

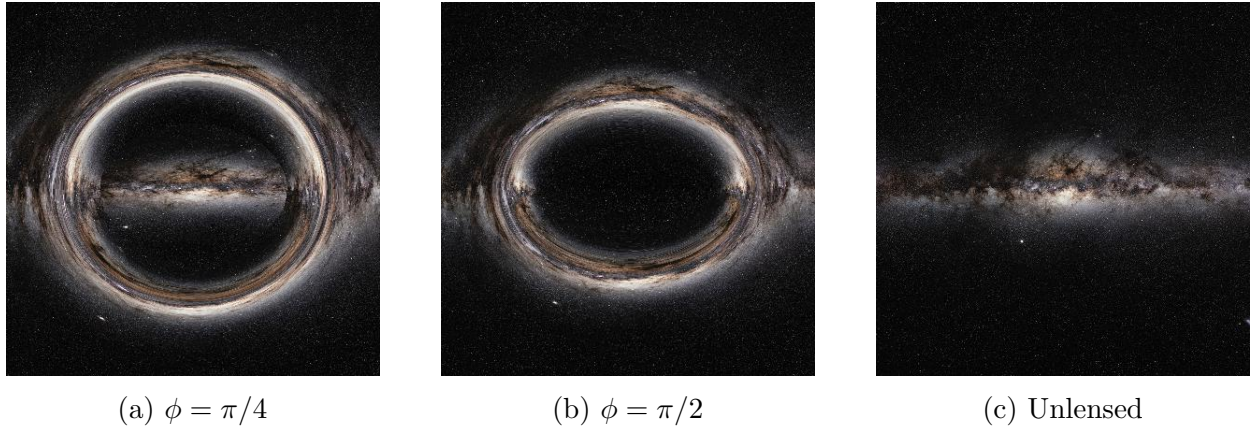
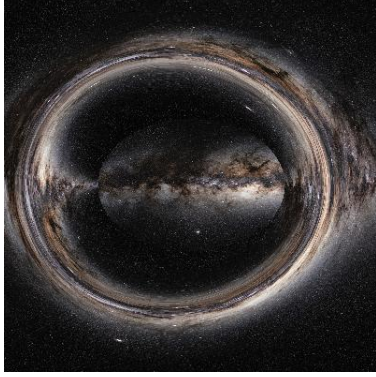


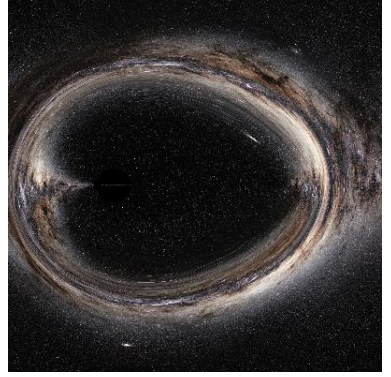
FIG. 13: Illustration of the milky way center lensed by circular cosmic string loop at  $\phi = \pi/4$  (a),  $\phi = \pi/2$  (b), and the unlensed image (c).



FIG. 14: Lensing Image of circular vorton at  $\phi = \pi/4$  (a) and  $\phi = \pi/2$  (b).



(a)  $\phi = \pi/4$



(b)  $\phi = \pi/2$

FIG. 15: Illustration of the milky way center lensed by circular vorton at  $\phi = \pi/4$  (a) and  $\phi = \pi/2$  (b).

The vector components and magnitude are shown as two-dimensional density plots in Figs. 16-17, respectively. As before, we observe a dominant deflection region despite the symmetry of the string projection. This comes from from the photon counteracting the frame-dragging effect, which acts in the opposite direction.

The image magnifications from the Kibble-Turok vorton are shown in Fig. 18. We can observe that there can be multiple regions of high magnification, where both inverted and non-inverted images inside the loop projection are visible. Fig. 19 displays the critical curves and caustics for several values of  $\kappa$ . Notably, multiple critical curves can be seen, with additional critical curve appearing within the string loop region. This discontinuity arises from the thin-string approximation and would be smoothed out if the approximation were relaxed.

Finally, the lensing images are presented in Fig. 20, while Fig. 21 illustrates the lensing effect on the Milky Way. As before, the frame-dragging effect produces visible asymmetry of the Einstein ring in 21, despite the symmetry of the projected string geometry. Note that the string loop is not fully contained within the lensing plane, as can be seen in Fig. 1.

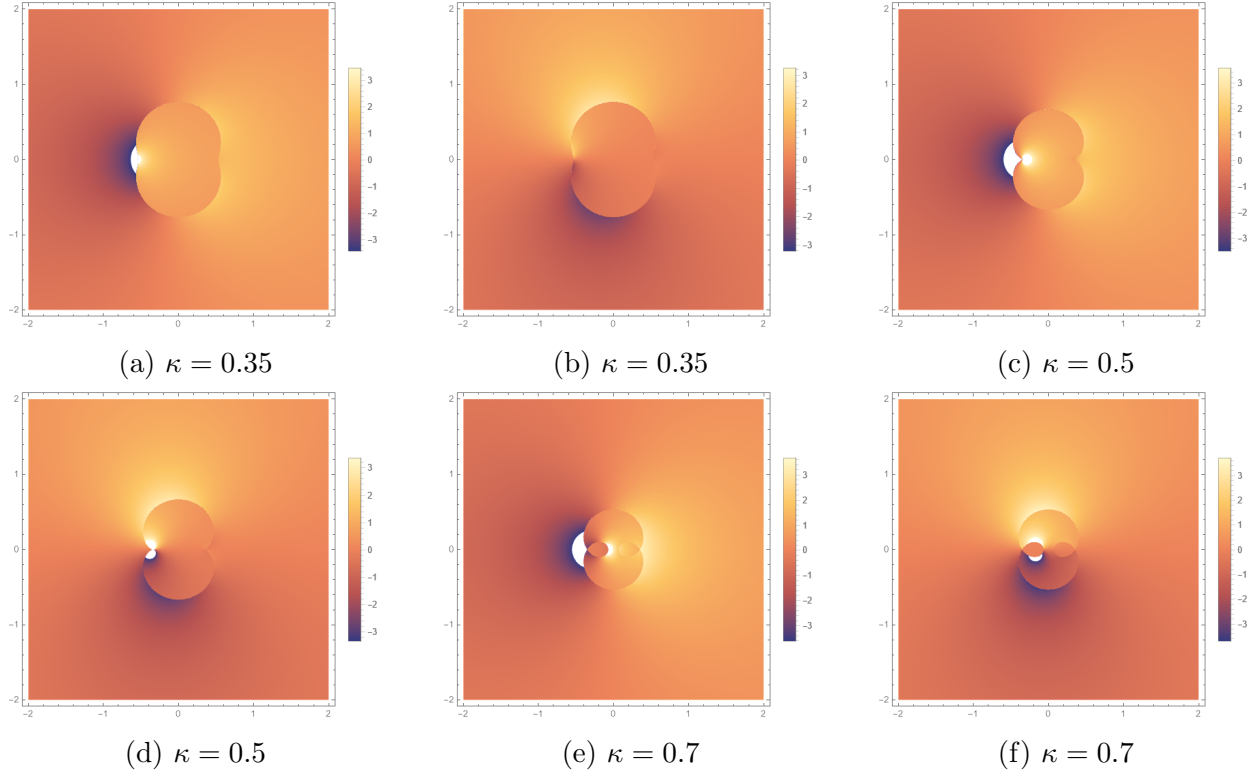


FIG. 16: Deflection vector component  $F_1$  (a, c, e) and  $F_2$  (b, d, f) from Kibble-Turok vorton of various  $\kappa$ .

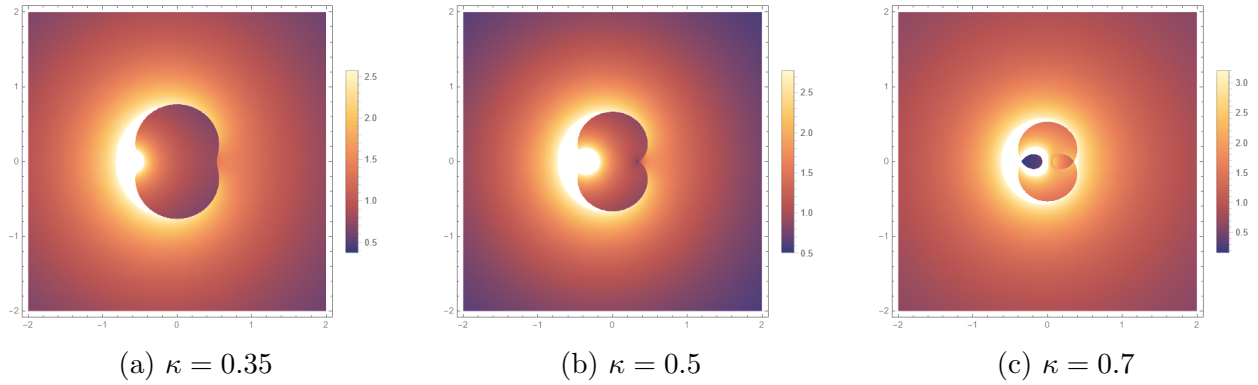


FIG. 17: Deflection vector magnitude  $|\vec{F}| = \sqrt{F_1^2 + F_2^2}$  from Kibble-Turok vorton of various  $\kappa$ .

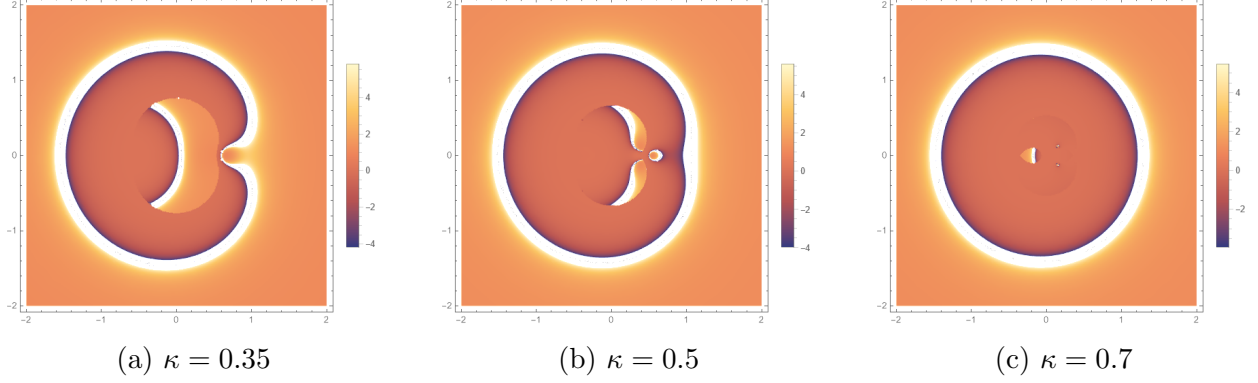


FIG. 18: Magnification by Kibble-Turok vorton for various  $\kappa$ .

#### D. The 123-Vorton

Using the same re-definition for  $\theta$  as before gives us the deflection vectors of the 123-vorton

$$F_1(x_1, x_2) = -\frac{1}{\pi} \int_0^{2\pi} d\theta \left[ \left( 1 - \frac{W}{1-W} \right) \frac{\sqrt{\beta}(1-\kappa) \sin \theta + \frac{1}{3}\kappa \sin 3\theta - x_1}{(\sqrt{\beta}(1-\kappa) \sin \theta + \frac{1}{3}\kappa \sin 3\theta - x_1)^2 + \mathcal{R}_2^2} \right], \quad (47)$$

$$F_2(x_1, x_2) = \frac{1}{\pi} \int_0^{2\pi} d\theta \left[ \left( 1 - \frac{W}{1-W} \right) \times \frac{\sqrt{\beta}(1-\kappa) \cos \theta - \frac{1}{\sqrt{2}}\sqrt{1-2\beta-\kappa^2} \sin 2\theta - \sqrt{\frac{\beta}{2}} \cos 2\theta + \frac{1}{3}\kappa \cos 3\theta + x_2}{(\sqrt{\beta}(1-\kappa) \sin \theta + \frac{1}{3}\kappa \sin 3\theta - x_1)^2 + \mathcal{R}_2^2} \right], \quad (48)$$

with

$$W \equiv \frac{1 - 2 \left( \sqrt{\beta} \sqrt{\kappa(1-\kappa)} \sin \theta - \sqrt{\beta/2} \kappa \sin 2\theta \right)}{1 - \left( \sqrt{\beta} \sqrt{\kappa(1-\kappa)} \sin \theta - \sqrt{\beta/2} \kappa \sin 2\theta \right)},$$

$$\mathcal{R}_2 \equiv \sqrt{\beta}(1-\kappa) \cos \theta - \frac{1}{\sqrt{2}}\sqrt{1-2\beta-\kappa^2} \sin 2\theta - \sqrt{\frac{\beta}{2}} \cos 2\theta + \frac{1}{3}\kappa \cos 3\theta + x_2. \quad (49)$$

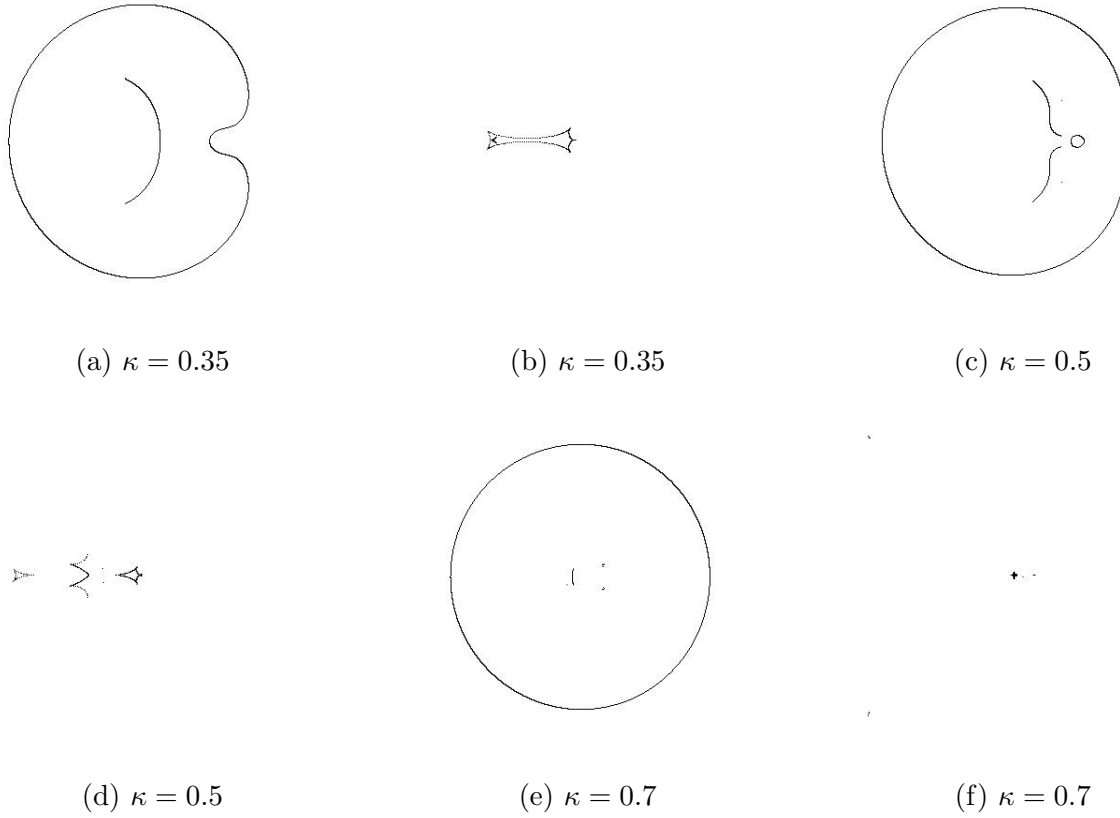


FIG. 19: Critical (a, c, e) and caustics (b, d, f) curves of the Kibble-Turok vorton of various  $\kappa$ .

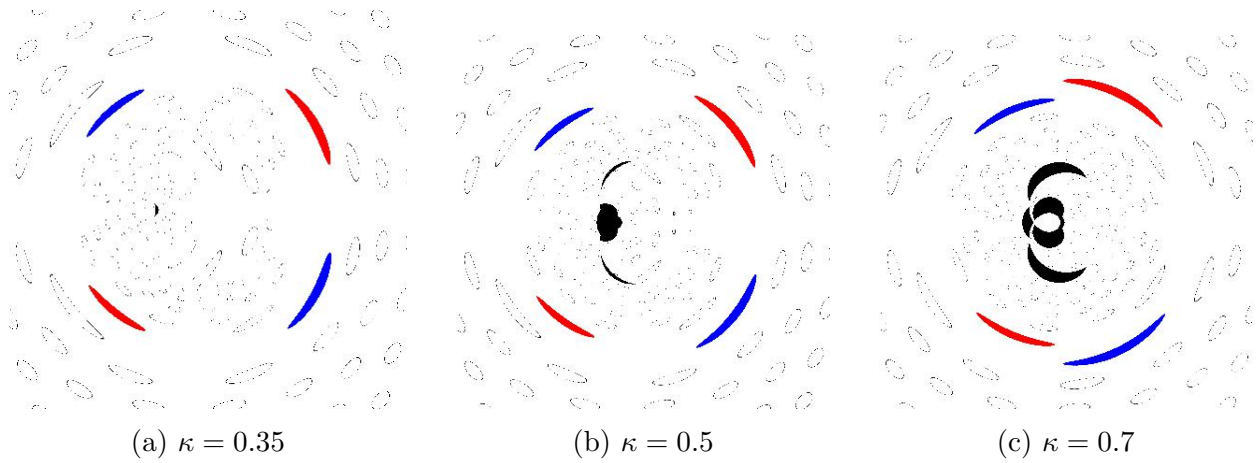


FIG. 20: Lensing Image of Turok vorton for various value of  $\kappa$ .



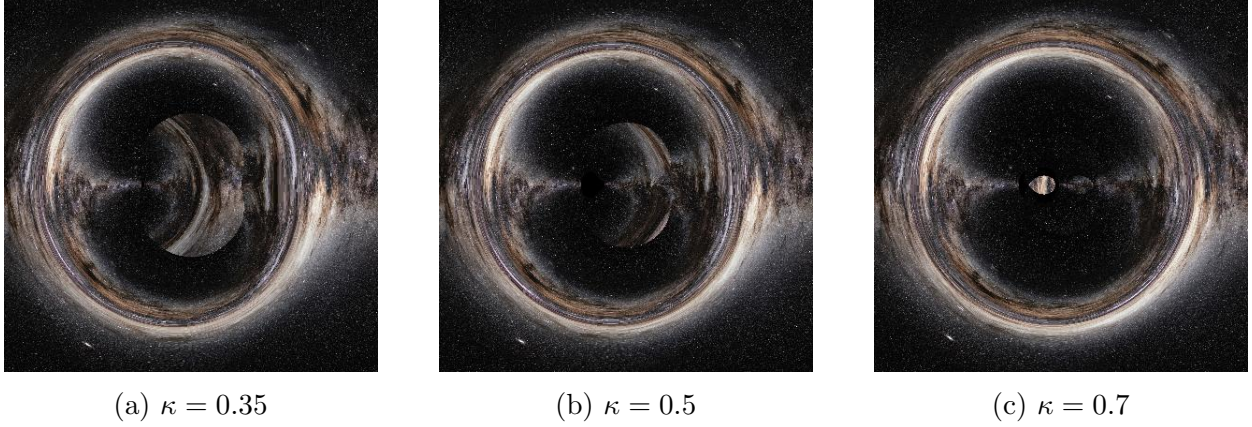


FIG. 21: Illustration of the milky way center lensed by Turok vorton for various value of  $\kappa$ .

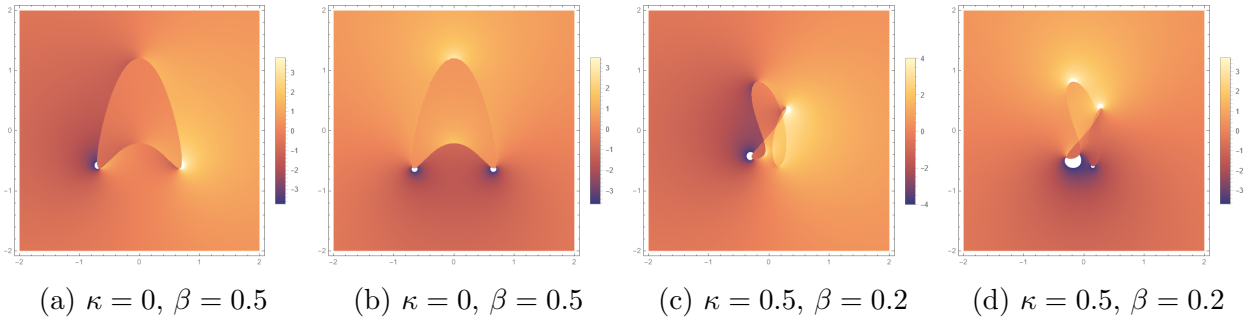


FIG. 22: Deflection vector component  $F_1$  (a, c) and  $F_2$  (b, d) of the 123 vorton of various  $\kappa$  and  $\beta$ .



FIG. 23: Deflection vector magnitude  $|\vec{F}| = \sqrt{F_1^2 + F_2^2}$  of the 123 vorton of various  $\kappa$  and  $\beta$ .

The components and magnitudes of the vector are shown represented as density plots in Figs. 22 and 23, respectively. Unlike the cases before, the projected curve of the string for  $\kappa = 0, \beta = 0.5$  is the actual vorton curve, as it lies completely on the lens plane. As the

result, the effect of frame dragging would be irrelevant in this case. However, we could still see some peaks of deflection on the image. This is not due to the frame dragging effect (as is the case in the  $\kappa = 0.5$ ,  $\beta = 0.2$  case), but the result of the locally peaked curvature of the string, which yields locally high energy density. This effect can also be observed in the  $\kappa = 0.5$ ,  $\beta = 0.2$  case, however it is not present in the circular loop case, because the highly curved segments of the projected curve are only an apparent one, as the true shape of the loop is circular, which has uniform curvature.

The magnification density plots are displayed in Fig. 24. As in previous cases, there are multiple regions with both inverted and non-inverted images, observable within the discontinuity of the loop's projected curve. The corresponding critical and caustics curves are shown in Fig. 25, where they appear perfectly symmetric, as does the string projection in Fig. 2b also being symmetric. This is because the vorton loop is perfectly inside the lensing plane. Consequently, there is no frame-dragging effect around an axis perpendicular to the optical axis, and the frame-dragging effect around the optical axis itself is negligible within this approximation.



FIG. 24: Magnification by the 123 vorton for several values of  $\kappa$  and  $\beta$ .

The lensing images along with its simulated effect on the Milky Way are shown in Figs. 26 and 27, respectively, for several different values of  $\kappa$  and  $\beta$ . As previously discussed, lensing effects such as the Einstein ring are evident in Fig. 27a, along with the pronounced symmetry visible in Fig. 26. The discontinuity on the string, projected onto the image plane, is also clearly apparent. Other generic properties of lensing images, such as shear, is also present consistently across all images produced by all types of vorton and cosmic string discussed here. However, we note that in order to observe these discontinuities, the vorton ought to



have at least a galaxy behind it, and that the vorton is of the angular size resolvable to telescope.

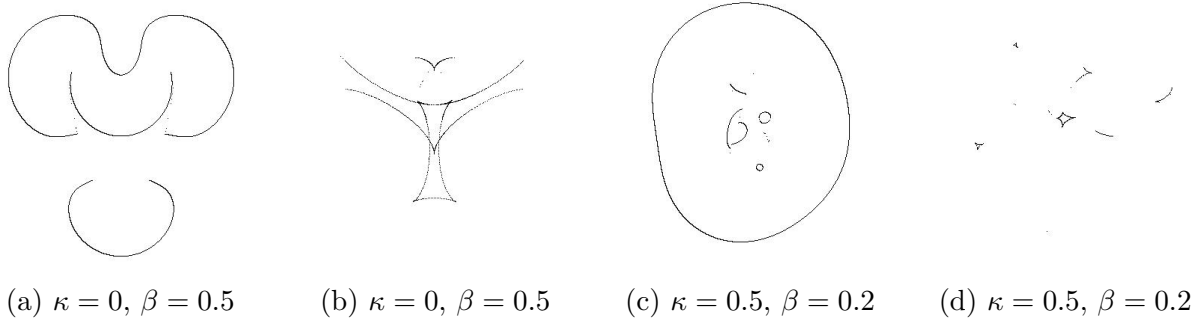


FIG. 25: Critical (a, c) and caustics (b, d) curves of the 123 vorton of various  $\kappa$  and  $\beta$ .



FIG. 26: Lensing images of the 123 vorton for various value of  $\kappa$  and  $\beta$ .



FIG. 27: Illustration of the milky way center lensed by the 123 vorton for various value of  $\kappa$  and  $\beta$ .

## IV. CONCLUSIONS

In our previous work [26], we analyzed the lensing patterns of a circular chiral vorton by deriving its metric and studying the associated null geodesics. In this study, we extend our analysis to arbitrary vorton shapes. We derive stationary solutions to the Nambu-Goto equations, describing non-circular vorton loops with arbitrary harmonic modes, and investigate their lensing effects. However, this generalization comes at the expense of an explicit metric solution. To overcome this limitation, we adopt the thin-lens approximation, where we treat the contribution of the string to the metric is weak and can thus be treated as a perturbation on a flat background [17].

There are a few unique and notable properties of the images generated by chiral vorton. For instance, as shown in Fig. 14, the lensed images from a circular vorton have an apparent discontinuity, separating a minimally distorted region from a highly distorted ones, both originating from the same source. An Einstein ring can form around a vorton, while the original source image remains visible at the center of the ring with relatively minimal distortion, as illustrated in Fig. 15. The simultaneous appearance of both the Einstein ring and an almost undistorted source image may be a phenomenon unique to cosmic string loops, offering a potential method for identifying such objects in nature. For non-circular vorton, the image at the center of the ring exhibits greater distortion, as illustrated in Fig. 27.

The effects of frame dragging are evident in certain configurations and shapes of chiral vorton solutions (Figs. 14, 20, and 26), where discontinuities in the string are also present (Figs. 15, 21, and 27). The frame-dragging effects can break the symmetry of images produced by a symmetric lens. This behavior contrasts with NG strings, which produce symmetric lensing images due to the absence of frame dragging. These distinctive features make chiral vortons identifiable through direct observation. For vortons with larger angular sizes, gravitational lensing could serve as a reliable method for detection.

As a final remark, it is worth noting that non-circular vortons have, thus far, only been constructed for vortons with chiral currents. Whether other superconducting string models, such as the Witten model, can produce non-circular vorton solutions remains an open question.

## Acknowledgments

We thank Steven Holme and Jose Blanco-Pillado for the discussions on the dynamics of vortons and its cosmological signatures, respectively. This work is funded by the Hibah Riset FMIPA UI No. PKS-042/UN2.F3.D/PPM.00.02/2024.

- 
- [1] E. D. Miner, R. R. Wessen, and J. N. Cuzzi, “Planetary Ring Systems,” Springer Praxis, Chichester (2007).
  - [2] M. S. Tiscareno, “Planetary Rings,” In: T. D. Oswalt, L. M. French, P. Kalas (eds) Planets, Stars and Stellar Systems, Springer, Dordrecht (2013).
  - [3] O. D. Kellogg, “Foundations of Potential Theory,” New York: Dover Pub. Inc. (1929).
  - [4] J. C. Maxwell, “On the stability of the motion of Saturn’s rings,” *Mon. Not. R. Astron. Soc.* **19** (1859), 297-304.
  - [5] R. A. Broucke and A. Elipe, “The dynamics of orbits in a potential field of a solid circular ring,” *Regul. Chaotic Dyn.* **10** (2005), 2, 129-143.
  - [6] A. Vilenkin, “Cosmic Strings and Domain Walls,” *Phys. Rept.* **121** (1985), 263-315.
  - [7] A. Vilenkin and E. P. S. Shellard, “Cosmic Strings and Other Topological Defects,” Cambridge University Press, 2000, ISBN 978-0-521-65476-0.
  - [8] V. P. Frolov, W. Israel and W. G. Unruh, “Gravitational Fields of Straight and Circular Cosmic Strings: Relation Between Gravitational Mass, Angular Deficit, and Internal Structure,” *Phys. Rev. D* **39** (1989), 1084-1096.
  - [9] S. J. Hughes, D. J. McManus and M. A. Vandyck, “Weak field gravity of circular cosmic strings,” *Phys. Rev. D* **47** (1993), 468-473. [arXiv:gr-qc/9211011 [gr-qc]].
  - [10] D. J. McManus and M. A. Vandyck, “Weak field gravity of revolving circular cosmic strings,” *Phys. Rev. D* **47** (1993), 1491-1496. [arXiv:gr-qc/9212007 [gr-qc]].
  - [11] Y. Nambu, Lectures at the Copenhagen Summer Symposium, 1970 (unpublished).
  - [12] T. Goto, “Relativistic quantum mechanics of one-dimensional mechanical continuum and subsidiary condition of dual resonance model,” *Prog. Theor. Phys.* **46** (1971), 1560-1569.
  - [13] T. W. B. Kibble and N. Turok, “Selfintersection of Cosmic Strings,” *Phys. Lett. B* **116** (1982), 141-143

- [14] N. Turok, “Grand Unified Strings and Galaxy Formation,” Nucl. Phys. B **242** (1984), 520-541
- [15] A. L. Chen, D. A. DiCarlo and S. A. Hotes, “Selfintersections in a Three Parameter Space of Cosmic Strings,” Phys. Rev. D **37** (1988), 863
- [16] D. B. DeLaney and R. W. Brown, “A Product Representation for the Harmonic Series of a Unit Vector: A String Application,” Phys. Rev. Lett. **63** (1989), 474
- [17] A. A. de Laix and T. Vachaspati, “Gravitational lensing by cosmic string loops,” Phys. Rev. D **54** (1996), 4780-4791 [arXiv:astro-ph/9605171 [astro-ph]].
- [18] R. L. Davis and E. P. S. Shellard, “COSMIC VORTONS,” Nucl. Phys. B **323** (1989), 209-224.
- [19] J. J. Blanco-Pillado, K. D. Olum and A. Vilenkin, “Dynamics of superconducting strings with chiral currents,” Phys. Rev. D **63** (2001), 103513 [arXiv:astro-ph/0004410 [astro-ph]].
- [20] A. C. Davis, T. W. B. Kibble, M. Pickles and D. A. Steer, “Dynamics and properties of chiral cosmic strings in Minkowski space,” Phys. Rev. D **62** (2000), 083516 [arXiv:astro-ph/0005514 [astro-ph]].
- [21] C. J. A. P. Martins and E. P. S. Shellard, “Vorton formation,” Phys. Rev. D **57** (1998), 7155-7176 [arXiv:hep-ph/9804378 [hep-ph]].
- [22] R. A. Battye and P. M. Sutcliffe, “Vorton construction and dynamics,” Nucl. Phys. B **814** (2009), 180-194. [arXiv:0812.3239 [hep-th]].
- [23] B. Carter, “Mechanics of cosmic rings,” Phys. Lett. B **238** (1990), 166-171 [arXiv:hep-th/0703023 [hep-th]].
- [24] Y. Lemperiere and E. P. S. Shellard, “Vorton existence and stability,” Phys. Rev. Lett. **91** (2003), 141601 [arXiv:hep-ph/0305156 [hep-ph]].
- [25] B. Carter and X. Martin, “Dynamic instability criterion for circular (Vorton) string loops,” Annals Phys. **227** (1993), 151-171 [arXiv:hep-th/0306111 [hep-th]].
- [26] L. B. Putra and H. S. Ramadhan, “Gravitational field and lensing of a circular chiral vorton,” [arXiv:2407.05270 [gr-qc]].
- [27] B. Carter and P. Peter, “Dynamics and integrability property of the chiral string model,” Phys. Lett. B **466** (1999), 41-49 [arXiv:hep-th/9905025 [hep-th]].
- [28] K. S. Virbhadra and G. F. R. Ellis, “Schwarzschild black hole lensing,” Phys. Rev. D **62** (2000), 084003 [arXiv:astro-ph/9904193 [astro-ph]].
- [29] P. Schneider, J. Ehlers and E. E. Falco, “Gravitational Lenses,” Springer, 1992, ISBN 978-3-540-66506-9, 978-3-662-03758-4.